Mon. Not. R. Astron. Soc. **000**, 1–15 (2011)   Printed 26 October 2011   (MN LaTeX style file v2.2)

Star cluster evolution in barred disc galaxies. I. Planar periodic orbits

I. Berentzen [1,2,3]⋆ and E. Athanassoula [3]†
[1] *Astronomisches Rechen-Institut, Zentrum für Astronomie, Universität Heidelberg, Mönchhofstraße 12-14, 69120 Heidelberg, Germany*
[2] *Heidelberg Institute for Theoretical Studies, Schlosswolfsbrunnenweg 35, 69118 Heidelberg, Germany*
[3] *Laboratoire d'Astrophysique de Marseille (LAM), UMR6110, CNRS/Université de Provence, Technopôle de l'Etoile, 38 rue Frédèric Joliot-Curie, 13388 Marseille Cédex 20, France*

arXiv:1110.5362v1 [astro-ph.GA] 24 Oct 2011

Accepted 2011 October 6. Received 2011 October 6; in original form 2011 September 4

ABSTRACT

The dynamical evolution of stellar clusters is driven to a large extent by their environment. Several studies so far have considered the effect of tidal fields and their variations, such as, e.g., from giant molecular clouds, galactic discs, or spiral arms. In this paper we will concentrate on a tidal field whose effects on star clusters have not yet been studied, namely that of bars. We present a set of direct N-body simulations of star clusters moving in an analytic potential representing a barred galaxy. We compare the evolution of the clusters moving both on different planar periodic orbits in the barred potential and on circular orbits in a potential obtained by axisymmetrising its mass distribution. We show that both the shape of the underlying orbit and its stability have strong impact on the cluster evolution as well as the morphology and orientation of the tidal tails and the sub-structures therein. We find that the dissolution time-scale of the cluster in our simulations is mainly determined by the tidal forcing along the orbit and, for a given tidal forcing, only very little by the exact shape of the gravitational potential in which the cluster is moving.

Key words: methods: N-body simulations – galaxies: star clusters, - Galaxy: open clusters and associations: general

1 INTRODUCTION

While the internal dynamical evolution of star clusters is mainly driven by relaxation processes, the global galactic environment in which they are hosted can drive their evolution externally. Different aspects of star cluster evolution in the gravitational field of galaxies have been studied numerously using numerical simulations. Recent direct N-body simulations include the effects of the Galactic tidal field (Küpper et al. 2008; Ernst et al. 2009) and dynamical friction terms for clusters close to the galactic centre (Just et al. 2011). From such kind of simulations the picture emerged that star clusters steadily loose stars through the Lagrangian points in the system and form long tidal tails. In axisymmetric potentials the stars in these tails are found to follow orbits which can be approximated by epicycles, resulting in a cycloidal motion of stars along the tails when seen in the tidal tail coordinate system as introduced by Ernst et al. (2009). This results in the formation of sub-structures within the tidal tails in form of clumps, often referred to as *epicyclic over-densities.* Numerical simulations have also shown that such structures persist also in tails of star clusters on non-circular orbits, however, their local density and position with respect to the cluster in this case vary with time (Just et al. 2011; Küpper et al. 2010).

A detailed understanding of the formation, morphology and dynamics of tidal tails resulting from tidally disrupted dwarf galaxies and star clusters in galaxies are of great interest to observations especially in the Milky Way (e.g., Odenkirchen et al. 2001; Belokurov et al. 2006; Grillmair 2009, etc.), but also in other galaxies (e.g., Peng et al. 2002; Martínez-Delgado et al. 2009, 2010, etc.). Tidal streams are of particular interest for tracing the gravitational potential by reconstruction the orbits of the clusters, as e.g., for Palomar 5 (Odenkirchen et al. 2001). The underlying assumption for this method is that the tidal tails accurately trace the cluster orbit (Varghese et al. 2011).

The galactic potentials used in numerical simulations such as the ones mentioned above are usually confined to sphericity or axisymmetry for simplicity. However, disc galaxies such as the Milky Way show a variety of morphological and dynamical sub-structures that are known to affect the evolution of star clusters. E.g., the effect of inter-

---

⋆ E-mail: iberent@ari.uni-heidelberg.de (IB)
† E-mail: lia@oamp.fr (EA)

actions with giant molecular clouds and spiral arm passages on the cluster dissolution time-scale has been studied by Gieles et al. (2006) and Gieles et al. (2007), respectively.

In this work we focus on the evolution of star clusters in the time-dependent gravitational potential of barred disc galaxies. Stellar bars are known to be the main internal driver of disc galaxy evolution and are strong non-linear perturbations to the gravitational potential of disc galaxies, thus having strong effects on the underlying orbital structure in both 2-d and 3-d. We present a set of direct N-body simulations of star clusters moving on planar periodic orbits in barred potentials and on circular orbits in (near-) axisymmetric potentials. We particularly focus on the formation and evolution of tidal tails in both scenarios.

The paper is structured as follows: In Section 2 we describe the numerical methods and initial conditions used in our N-body simulations. Section 3 then describes the results. We give conclusions in Section 4.

2 NUMERICAL METHODS AND INITIAL CONDITIONS

2.1 Direct N-body code using GPU clusters

We use a modified version of the publicly available direct N-body code φ-GRAPE (Harfst et al. 2007). It provides hierarchical particle time-steps and a fourth order Hermite integration scheme (e.g., Makino et al. 1992). Originally, this code is written for high-performance computing clusters equipped with the special-purpose hardware GRAPE-6 (Makino et al. 2003; Fukushige et al. 2005) to accelerate the gravitational force calculation. It has been used in the past for simulations of dense stellar systems such as galactic nuclei (e.g., Berczik et al. 2005, 2006; Berentzen et al. 2009; Kharchenko et al. 2009). In our current version, the code has been adjusted to run on Graphic Processing Units (GPUs) using the SAPPORO library (Gaburov et al. 2009) which allows to use the GPU cards like the special-purpose hardware GRAPE.

There are alternative direct N-body codes freely available with more advanced features, such as regularisation methods for an accurate integration of binaries, stellar evolutionary tracks for single and binary stars, etc. However, the present work is the first to study star cluster evolution in barred galaxies and therefore we restrict ourselves to relatively simple models. Simulations with higher resolution, particle mass functions and increasingly more input physics will be studied in the future.

In order to prevent the formation of stellar binaries or multiples in our simulations, we adopt a small gravitational (Plummer) softening in the force calculation. As a trade-off we study the evolution of the star clusters in the pre core-collapse phase only, where binaries and multiples are of less dynamical importance. As mentioned before, we limit ourselves in this work to N-body models with equal mass particles. This prevents some possible dynamical effects such as mass segregation (see, e.g., Khalisi et al. 2007). We also neglect the dynamical friction between the star cluster and the galaxy, which generally becomes important close to the galactic centre. We discuss the possible effects of this limitation when necessary and leave simulations including this extra physics for the future.

In the next subsection we describe the analytic galaxy model that we have implemented in the φ-GRAPE as an external potential and force field.

2.2 Analytic barred galaxy model

We use an analytic three-component galaxy model which is composed of an axisymmetric disc, a spherically symmetric bulge/halo and a triaxial bar component. The disc potential $\Phi_{\rm D}$ in our model is represented by a three dimensional Miyamoto-Nagai potential (Miyamoto & Nagai 1975) of the form

$$\Phi_{\rm MN}(x,y,z) = \frac{GM_0}{\sqrt{x^2+y^2+\left(A+\sqrt{B^2+z^2}\right)^2}} \ , \qquad (1)$$

where G is the gravitational constant, M_0 is the total mass of the component, and A and B are the radial and vertical scale-length, respectively.

The spherically symmetric bulge/halo potential $\Phi_{\rm B}$ of our galaxy model is represented by a Plummer potential (Plummer 1911), i.e., also described by Eq. 1 with $A = 0$. For the bar potential $\Phi_{\rm bar}$ we use a three-dimensional Ferrers' ellipsoidal potential (Ferrers 1877) which is based on a density distribution of the form

$$\rho(x,y,z) = \begin{cases} \frac{105\,M_{\rm bar}}{32\pi\,a_{\rm bar}\,b_{\rm bar}\,c_{\rm bar}}\,(1-m^2)^2 & \text{if } m \leqslant 1 \\ 0 & \text{if } m > 1 \end{cases} \qquad (2)$$

with

$$m^2 = \frac{x^2}{a_{\rm bar}^2} + \frac{y^2}{b_{\rm bar}^2} + \frac{z^2}{c_{\rm bar}^2} \qquad \text{and } a_{\rm bar} > b_{\rm bar} > c_{\rm bar} \ , \quad (3)$$

where $M_{\rm bar}$ is the mass of the bar component and $a_{\rm bar}$, $b_{\rm bar}$ and $c_{\rm bar}$ are its semi-principal axes. Note that in our description the bar major axis is aligned with the x-axis of our coordinate system. The full analytic expressions of the gravitational potential $\Phi_{\rm bar}$ and corresponding forces can be found in Pfenniger (1984).

The fourth order Hermite integration scheme used in our code requires both the particle acceleration $\mathbf{a}_i$ and its time derivative $\mathbf{j}_i$ (also called 'jerk'). We integrate the evolution of the star cluster in a reference frame which is co-rotating with the bar, with a constant pattern speed $\Omega_{\rm bar}$. The resulting equations of motion for a particle are then given by, e.g., Binney & Tremaine (1984):

$$\boldsymbol{a}_i = \boldsymbol{a}_{\rm cl} - \boldsymbol{\nabla}\Phi_{\rm gal} - 2\left(\boldsymbol{\Omega}_{\rm bar}\times\dot{\boldsymbol{r}}_i\right) - \boldsymbol{\Omega}_{\rm bar}\times\left(\boldsymbol{\Omega}_{\rm bar}\times\boldsymbol{r}_i\right) \ , \quad (4)$$

where $\boldsymbol{a}_{\rm cl}$ is due to the self-gravity of the stellar cluster, $\Phi_{\rm gal} = \Phi_{\rm D} + \Phi_{\rm B} + \Phi_{\rm bar}$ and the last two terms are the Coriolis and centrifugal force, respectively. The jerk is then given as:

$$\boldsymbol{j}_i = \boldsymbol{j}_{\rm cl} - \frac{\partial}{\partial t}\boldsymbol{\nabla}\Phi_{\rm gal} - 2\left(\boldsymbol{\Omega}_{\rm bar}\times\boldsymbol{a}_i\right) - \boldsymbol{\Omega}_{\rm bar}\times\left(\boldsymbol{\Omega}_{\rm bar}\times\dot{\boldsymbol{r}}_i\right) \ . \quad (5)$$

For the N-body realisation of the star clusters we use distribution functions following a Plummer density profile (Plummer 1911) or a King density profile (King 1966). We found no qualitative differences in the evolution between

Table 1. Galaxy model parameter in model units.

Component	M_0 [$\times 10^4$]	A [$\times 10^3$]	B [$\times 10^3$]
disc	16.4	3.0	1.0
bulge/halo	1.6	–	0.4

M_0 is the mass of the components given in the first column. A and B are the radial and vertical scaling parameters of the Miyamoto-Nagai potential.

Table 2. Bar model parameters in model units.

Component	$M_{\rm bar}$	$a_{\rm bar}$	$b_{\rm bar}$	$c_{\rm bar}$
bar	2×10^4	6×10^3	1.5×10^3	0.6×10^3

$M_{\rm bar}$ is the mass of the bar component. $a_{\rm bar}$, $b_{\rm bar}$ and $c_{\rm bar}$ are the bar's semi-principal axes.

the two types of models in our set of simulations. Since our simulations with King models have been run with a higher particle number and also have been carried out to longer simulation times we limit ourselves in this publication to those models. To set up the (non-rotating) isotropic King model for a given core radius $r_{\rm c}$ and central concentration W_0 we use Walter Dehnen's `mkking` routine from the open source NEMO software package (Teuben 1995).

All simulations presented in this work have been carried out on the dedicated GPU cluster KOLOB at the University of Heidelberg and at the GPU facilities at the Laboratoire d'Astrophysique de Marseille.

2.3 Parameter and units

We set the gravitational constant G to unity and the units of mass and length to $M_{\rm u} = 10^6\,{\rm M}_\odot$ and $R_{\rm u} = 1\,{\rm pc}$, respectively. With this choice, the resulting units of time and velocity become $\tau_{\rm u} = 15 \times 10^3\,{\rm yr}$ and $v_{\rm u} = 65.6\,{\rm kms}^{-1}$. Although the N-body models are intrinsically scale-free, one should bear in mind that both the galaxy and the star cluster must be scaled simultaneously when scaling to different units, e.g., physical units. Especially, a rescaling of the models will also change the bar pattern speed. Throughout this work we stay with the model units and refer to physical units only when necessary.

Our choice of model parameter is based on the well studied galaxy model described in Skokos et al. (2002a). The corresponding mass distribution in this model results in a rotation curve as typically observed for disc galaxies. The parameter converted to our set of units are given in Tables 1 and 2 for the galaxy and for the bar, respectively. The pattern speed of the bar is correspondingly set to $\Omega_{\rm bar} = 7.64 \times 10^{-4}$ rad $\tau_{\rm u}^{-1}$ with the bar rotating counterclockwise in the (non-rotating) lab-frame. The rotation period of the bar corresponds to $T_{\rm bar} \approx 8224\,\tau_{\rm u}$.

The parameters of the star cluster(s) are summarised in Table 3. The half-mass radius of our (isolated) 50000 (50k) particle King model corresponds to $r_{\rm h} \approx 4$ and the tidal radius to about $r_{\rm t} \approx 34$. The total energy of the N-body system is about $E_{\rm cl} = -2 \times 10^{-3}$.

Table 3. Star cluster parameters in model units.

N	$\rm M_{tot}$	$\rm W_0$	$r_{\rm c}$	ε
50000	0.2	7.0	1.0	0.001

N is the particle number used in the N-body model and $\rm M_{tot}$ is the total cluster mass. $\rm W_0$ and $\rm r_c$ are the concentration parameter and the core radius of the King profile, respectively, and ε is the gravitational softening length used in the simulations.

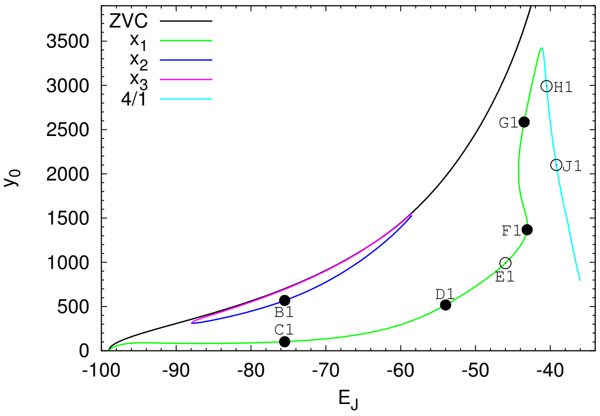

Figure 1. Characteristic diagram of our barred potential. We plot the y-intercepts (y_0) of the main planar prograde periodic orbits as a function of Jacobi energy $E_{\rm J}$. The black line is the zero-velocity curve (ZVC). The main periodic 2-d families are shown in different colours as given in the legend. We mark the orbits on which we evolve the star clusters, indicating the stability by filled (stable) and open circles (unstable).

2.4 Planar periodic orbits

In this work we place the star cluster in the mid-plane of the galactic disc on an orbit which is periodic in the co-rotating reference frame of the bar. These orbits are the backbone of stellar bars (in 2-d) because they can confine regular regions (invariant tori) in phase-space around them. Orbits located in these regions show similar shapes and characteristics as their underlying parent periodic orbit. Thus we would expect a similar evolution of the star cluster when placed on more general orbits.

In Fig. 1 we show the characteristic diagram for the main planar orbit families (see, e.g., Binney & Tremaine 1984) in the barred potential. We plot the y-axis intercepts (y_0, with $\dot{y} < 0$) of the periodic orbits as a function of their Jacobi integral, $E_{\rm J}$, which is given as $E_{\rm J} = E - J\,\Omega_{\rm bar}$. Here, E and J are, respectively, the specific energy and the angular momentum of the orbit. The Jacobi integral is a conserved quantity in the frame corotating with the bar[1].

The green line shows the so-called x_1 orbit family, following the nomenclature of Contopoulos & Papayannopoulos (1980). These orbits are elongated along the bar major axis and close after one revolution in the bar potential and two radial oscillations

---

[1] Due to the self-gravity of the N-body system the Jacobi integral is not a conserved quantity in our simulations.

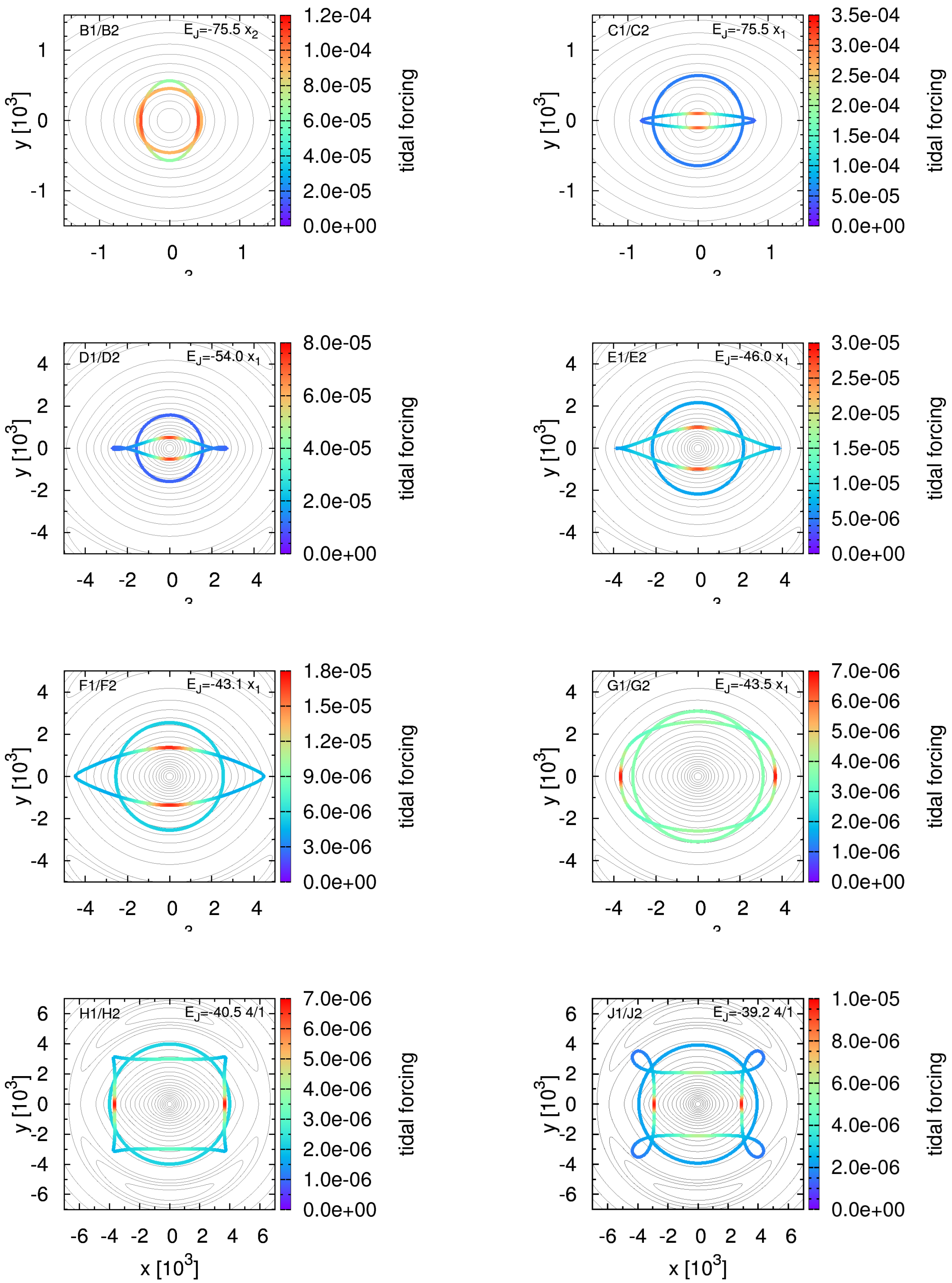

Figure 2. 2-d planar periodic orbits in the barred and the axisymmetric potential. The corresponding orbit name, Jacobi integral $E_{\rm J}$ (for the barred model) and family is given in each frame. The colour coding corresponds to the strength of the tidal forcing along the orbit. See main text (Section 3.4) for details. Iso-potential contours of the effective potential are plotted with grey lines.

(2/1). Close to the co-rotation radius the x_1 turns over to the four-periodic (4/1) orbit branch (cyan line). The blue and magenta line in Fig. 1 represent the so-called x_2 and x_3 orbit families, respectively. These orbits are a class of 2/1 orbits which are elongated perpendicular to the bar major axis and are a signature of the presence of the inner Lindblad resonance(s).

The set of orbits on which we place the star cluster in our simulations are marked and labelled in Fig. 1, where we indicate the stability using different symbols. A detailed discussion of the orbits and their stability in the potential used here is given in Skokos et al. (2002a).

For comparison, we also run a second set of simulations for each of the selected orbits, putting the star cluster on a circular orbit about the galactic centre using an (nearly) axisymmetric potential. For the latter, we maintain the mass of the bar, but set the parameter a in Eq. 3 to 2.7×10^3, which is the mean value of the three axes as given in Table 2. We then set $b = 0.99\,a$ and $c = 0.90\,a$ due to the required inequality of the three parameter (see Eq. 3). The axisymmetric galaxy components remain unchanged.

The radius of the circular orbits is determined as follows: we calculate the orbit-averaged radial acceleration $\overline{a_\mathrm{R}}$ on a test-particle in the barred potential[2] over one orbital period T_orb for each of the periodic orbits marked in Fig 1. Using a simple bi-section root-finding algorithm, we then determine the radius of the corresponding circular orbit which has the same mean radial force. Information about both kinds of orbits (barred and circular) and about our set of simulations is given in Fig. 2 and Table 4.

Table 4. Simulations

Orbit	E_J	family	y_0 $[10^3]$	T_orb
A	Isolation	–	–	–
B1	-75.5	x_2	0.57	812.3
B2	-75.2	circular	0.46	707.5
C1	-75.5	x_1	0.10	1041.4
C2	-68.5	circular	0.64	946.0
D1	-54.0	x_1	0.52	3178.8
D2	-49.1	circular	1.57	2111.0
E1	-46.0	x_1	0.99	4654.5
E2	-40.6	circular	2.17	2773.9
F1	-43.1	x_1	1.37	6075.4
F2	-36.6	circular	2.55	3262.1
G1	-43.5	x_1	2.59	8008.6
G2	-32.2	circular	2.09	3985.0
H1	-40.5	4/1	2.99	14733.1
H2	-26.3	circular	3.99	5167.0
J1	-39.2	4/1	2.10	14782.0
J2	-26.7	circular	3.92	5083.5

The first column gives the orbit name for each selected orbit. E_J is the Jacobi integral. The third column shows the corresponding orbit family. y_0 is the y-axis intercept of the orbit and T_orb is its orbital period.

3 RESULTS

In this section we describe the evolution of the star clusters first in isolation and then when placed initially on a periodic orbit in our barred potential. We also compare the results with simulations of star clusters on circular orbits in the corresponding axisymmetric potential. Many of the features described in this section are better seen in animation, than in plots. For this reason we include animations of all the models described here under `http://lam.oamp.fr/research/dynamique-des-galaxies/scientific-results/star-cluster-evolution/`.

3.1 Simulation A - isolated star cluster

Before studying the star cluster evolution in the gravitational field of our three-component galaxy model, we first run a simulation of the isolated cluster, i.e., without any external gravitational force.

In Fig. 3 we show the Lagrange radii, i.e., spherical radii that contain a fixed fraction of mass, as a function of time for the isolated 50k King model (cf. Table 3). We define the centre of the cluster as the centre of mass of all particles within a sphere of $r = 0.2$ around the particle with the highest mass denisty. The latter has been calculated using routines from the software package FALCON (Dehnen 2000, 2002). Due to close two- and few-body encounters between particles, its outer envelope slowly heats up and expands, while its inner regions simultaneously start to contract slowly. As can be seen from Fig. 3, the model does not undergo core collapse during the integration interval of 50000 time units, or some 750 Myr – i.e., roughly 5 bar rotations.

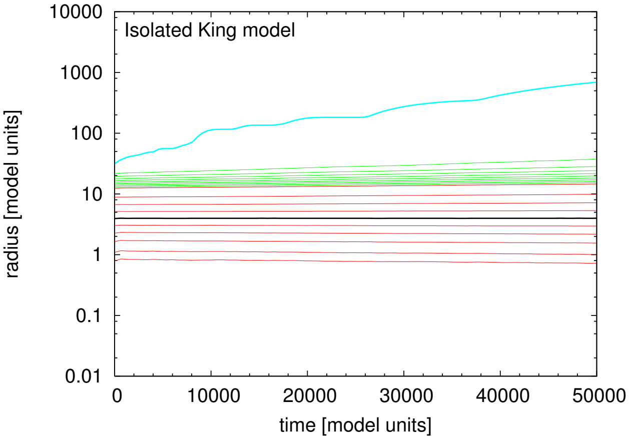

Figure 3. Lagrange radii as a function of time for the isolated 50k King model (simulation A). Red solid lines show mass fractions of 5, 10, 20, 30, . . . , 90 per cent of the total cluster mass and green solid lines are fractions of 91, 92, 93, . . . , 99 per cent (from bottom to top). The half-mass radius is plotted with a black solid line. The cyan solid line corresponds to the *farthest* gravitationally bound cluster particle, i.e., the particle with the largest distance to the cluster centre and a negative total energy.

We find that all stellar particles remain gravitationally bound to the isolated cluster until the end of the simulation.

---

[2] $\overline{a_\mathrm{R}} \equiv \frac{1}{N_j} \sum_{j=1}^{N_j} \mathbf{a}_j \cdot \mathbf{e}_{\mathrm{R},j}$, where $\mathbf{a}_j$ is the test particles acceleration at time $t_j = (j-1)\Delta t$ and $\mathbf{e}_{\mathrm{R},j}$ its normalised position vector. For a constant time-step Δt one gets $N_j = T_\mathrm{orb}/\Delta t + 1$.

This is most likely due to the small gravitational softening which prevents particles to reach escape velocities during close stellar encounters. The introduction of a gravitational softening in our models slightly reduces the strength of close particle encounters and prevents the formation of bound binaries. Since our simulations end clearly before core-collapse the dynamical impact of binaries can safely be neglected.

For this isolated King model the total energy E_{cl} of the cluster is a conserved quantity and can be used to check the accuracy of the numerical integration. We calculate the relative energy error and find that the energy is conserved to better than 5×10^{-3} per cent over the full integration time.

3.2 Periodic orbits - simulations B – J

In this subsection we present a mainly qualitative description of our simulations. We will use these results to quantify in the next subsection certain aspects of the cluster evolution and the formation and evolution of the tidal structures.

3.2.1 Simulations C1 and C2

The underlying orbit in simulation C1 belongs to the x_1 family (Figs. 1 and 2) and is dynamically stable. We place the cluster initially at pericentre at a distance from the galactic centre of about $R = y_0 = 100$ (Table 4) in the mid-plane of the disc. The cluster is then launched from pericentre with an initial centre of mass velocity according to this x_1 orbit. Since it is started relatively close to the centre of the galaxy, it is initially not in dynamical equilibrium – mainly due to the presence of strong tidal forces – and adjusts itself in the very early phases of evolution. This effect is visible in Fig. 4, in which we show the evolution of the Lagrange radii as a function of time for this simulation.

After its first apocentre passage at $t \approx 260$ the cluster starts to form tidal tails which become clearly pronounced for the first time after about half an orbital period (see Table 4). The leading and trailing tails are oriented along the underlying parent orbit and are initially confined to regions mainly inside and outside this orbit, separated by it. This is due to the fact that the particles are leaving the cluster – depending on their Jacobi integral – through the Lagrange points L_1 and L_2, where L_1 and L_2 lie between the cluster and the galactic centre and on the opposite cluster side, respectively (see Ernst et al. 2009, for an illustration).

When the cluster approaches again the orbital apocentre, the stars forming the leading tidal tail start to slow down following their pericentre passage. This leads to a “compression” first of the leading tidal tail, and consecutively of the cluster itself and of the trailing tidal tail as they approach the orbital apocentre and slow down as well. The compression of the tidal tails is reflected in a decrease of the Lagrange radii (Fig. 4), which become minimal each time the cluster just passed the orbital apocentre. In this phase the trailing tail is still undergoing compression due to its deceleration, while the leading tail starts to expand again. The expansion of the tidal tails is reflected in an increase of the Lagrange radii which reach their maxima when the cluster passes pericentre.

The effect of compression and expansion of the tidal features close to apocentre and pericentre passage has also been found in recent N-body simulations of star clusters moving on eccentric orbits in axisymmetric potentials (Küpper et al. 2010). The compression/expansion of tidal streams and the resulting asymmetry when close to apocentre should thus be inherent to clusters moving on non-circular orbits. The oscillations found in the Lagrange radii appear with the same period as the one of the periodic orbit and are therefore linked to the variations of the tidal field along the trajectory of the cluster.

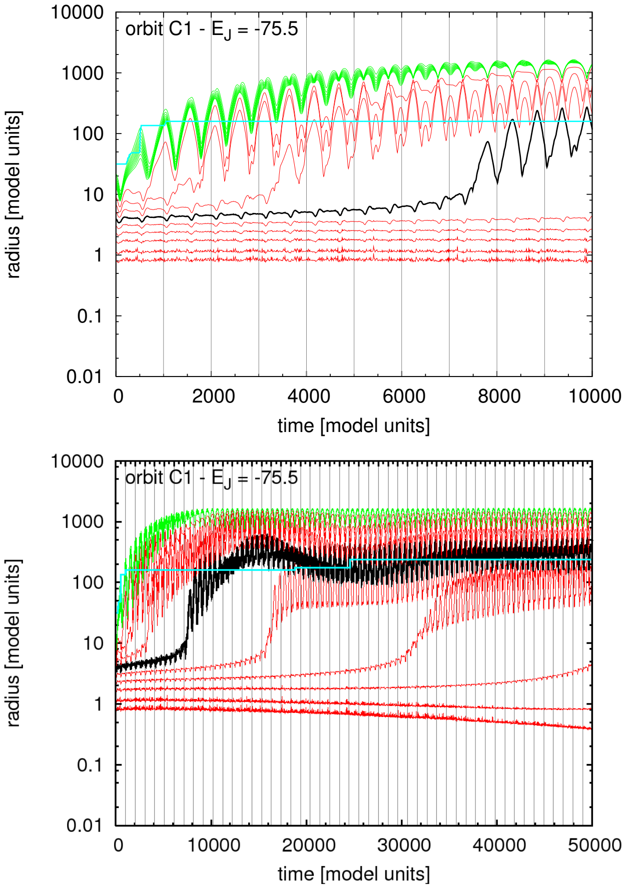

Figure 4. Lagrange radii of the cluster in simulation C1 (cluster on an x_1 orbit with $E_{\mathrm{J}} = -75.5$) as a function of time. The grey vertical lines indicate the orbital period in the bar reference frame. The top and bottom panels show the time evolution up to 10000 and 50000 time units, respectively. The layout of both panels is the same as in Fig. 3.

As expected, the effect of periodic compression and expansion is indeed not found in our corresponding simulation C2 in which the star cluster moves on a circular orbit in the axisymmetric potential. In this case the particles escape at an almost linear rate from the star cluster. For comparison with simulation C1 we show in Fig. 5 the time evolution of the Lagrange radii for our model C2. The expansion of the different mass shells is relatively smooth and does not show any oscillations such as those found in model C1. This is due to the fact that the star cluster moves along the circular orbit with almost constant azimuthal velocity and is exposed to a constant tidal field. Note that the radius of the farthest unbound cluster particle (see Fig. 5; cyan line) initially corresponds roughly to the initial tidal radius of the

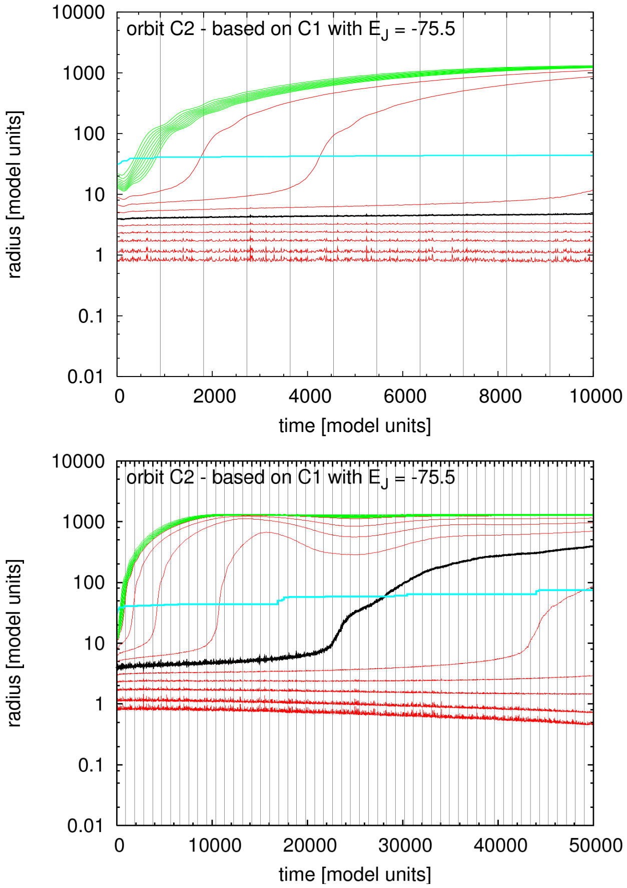

Figure 5. Lagrange radii for the simulation C2 (cluster on a circular orbit corresponding to orbit C1). Layout is the same as in Fig. 4. The sudden increase in the cyan line at around $t = 18000$ results from a particle getting ejected from the cluster and thus is no more the last bound particle.

cluster $r_{\rm t} = 35$, and slowly increases as the cluster is losing mass.

The maximum value for the Lagrange radii is given in both simulations, C1 and C2, by the separation of the two apocentres. We find in our run C1 that the tidal tails fill about half the length of the x_1 orbit after $t = 4880$, or roughly 5 orbital periods, and fills the full orbit at about $t = 7800$, or about 8 orbital periods.

In both simulations, C1 and C2, sub-structures form along the tidal tails in form of clumps (or *epicyclic overdensities*) as described and analysed in previous publications (Küpper et al. 2008; Ernst et al. 2009; Küpper et al. 2010). The position and strength of these clumps varies with the compression and expansion phases along the orbit. As the tidal tail reaches its maximum length at pericentre passage of the cluster, the relative clump density increases, i.e., shows the maximal density contrast between clumps and the tidal tails.

The periodic density variations of the tidal tails are visible also in the oscillations of the outer Lagrange radii (e.g., those corresponding to mass fractions larger than 90 per cent), with a period estimated by eye to about half the orbital period $T_{\rm orb}$ (see Fig. 4). To show that the density variations are indeed correlated to the orbital period of the parent periodic orbit we use a Fast Fourier Transformation (FFT) to determine the oscillation period from the time series of the Lagrange radius L_{98}, i.e., the radius which contains 98 per cent of the initial cluster mass. For our run C1 we find an oscillation period to be $T_{\rm L} = 529 \pm 1$, which in fact corresponds to roughly half the orbital period $0.5\,T_{\rm orb}$ of the x_1 orbit. Our results for this analysis are summarised in Table 5 for all periodic orbits presented here. We find that at the end of the simulation (after 50000 time units) the cluster in run C1 (barred potential) has lost about 79 per cent of its initial mass, while the same cluster in run C2 (circular orbit) has lost about 62 per cent of its initial mass.

Table 5. Periods.

Orbit	E_J	family	$T_{\rm orb}$	$T_{\rm L98}$	ratio
C1	-75.5	x_1	1041.4	529 ± 1	≈ 2
B1	-75.5	x_2	812.3	411 ± 1	≈ 2
D1	-54.0	x_1	3178.8	1743 ± 9	≈ 2
E1	-46.0	x_1	4654.5	2409 ± 18	≈ 2
G1	-43.5	x_1	8008.6	4096 ± 51	≈ 2
F1	-43.1	x_1	6075.4	3034 ± 28	≈ 2
H1	-40.5	4 : 1	14733.1	3682 ± 41	≈ 4
J1	-39.2	4 : 1	14782.0	3766 ± 43	≈ 4

The six columns, from first to last, give the orbit name, its Jacobi integral, the corresponding orbit family, its orbital period T$_{\rm orb}$, the period of the expansion/compression measured using the Lagrange radius L_{98} which contains 98 per cent of the initial cluster mass, respectively, and the ratio between the two periods.

3.2.2 Simulations B1 and B2

The parent periodic x_1 orbit in the previous simulation C1 is elongated along the major axis of the bar. We now describe the evolution of the cluster on an x_2 orbit with the same Jacobi integral of $E_{\rm J} = -75.5$, but which – in contrast to x_1 orbits – is oriented perpendicular to the bar major axis and is less eccentric. As before, this orbit is dynamically stable.

Qualitatively, the evolution of the star cluster on the x_2 orbit (run B1) and on the corresponding circular orbit are found to be similar to those in simulations C1 and C2, respectively. As in the previous simulations we find formation of tidal tails and sub-structures therein in both kinds of models, i.e., in both the barred and the axisymmetric potentials.

The effect of periodic compression/expansion of the tidal tails is less pronounced in run B1 (although clearly present) than in run C1 since the underlying x_2 orbit is less eccentric. This is also reflected in the amplitude of the oscillations (compare Fig. 6; left panel). Again, the successive compression and expansion of the tidal tails correlates with the orbital period of the x_2 orbit (see Table 5).

In simulation B2 (circular orbit) we note that the leading tidal tail and the trailing tidal tail are confined to regions inside and outside the underlying circular orbit owing to the particles epicyclic motion. Due to the strong non-linear perturbation of the bar in our simulation B1 the (linear) epicyclic approximation does not apply to the motion of the particles in the barred potential. As result of this we find a

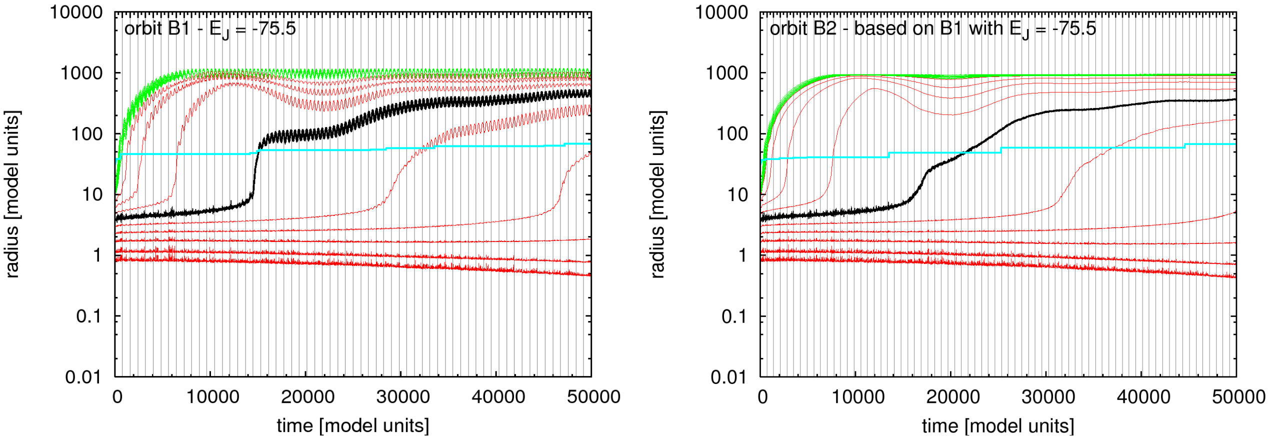

Figure 6. Lagrange radii for the simulation B1 (left panel; cluster on an x_2 orbit with $E_{\rm J} = -75.5$) and simulation B2 (right panel; corresponding circular orbit). The layout of both panels is the same as in Fig. 3.

higher fraction of particles crossing the underlying periodic orbit as compared to the circular orbit B2.

In simulation B1 the tidal tails fill one full orbit at about $t \approx 15000$. The mass loss of the initial cluster mass is about 73 percent in run B1 and about 69 percent in run B2. In subsection 3.4, we will quantify and discuss this difference in terms of the tidal field for all our simulations.

3.2.3 Simulations D1 and D2

In contrast to the previously described simulations, orbit D1 shows pronounced loops close to its apocentre (see Fig. 2), which is a clear signature for a strong bar (Athanassoula 1992). The orbit is stable but lies in the close vicinity of a short instability strip in the x_1 characteristic curve (see Fig.1).

We find that the formation and evolution of the tidal tails in simulations D1 and D2 is for several orbital periods qualitatively similar to that of cases with lower Jacobi integrals. Initially the forming tidal tails follow closely the underlying periodic orbit. After several apocentre passages of the cluster, however, we find that the tidal tails become a bit more diffuse compared to the previously described simulations. We attribute this effect to the dynamical stability of the periodic orbit. In the particular case of simulation D1 the underlying periodic orbit is dynamically stable. Particles in the tidal tails which leave the cluster, however, enter regions in phase space which correspond to an unstable periodic orbit and are thus not confined to the invariant tori of the initial parent orbit anymore.

As before, we find oscillations in the Lagrange radii (not shown here) whose period correlates with the orbital period of the D1 orbit (see Table 5). In Fig. 7 we show the cluster mass in run D1 as a function of time. Here we use two definitions of the cluster members, namely, (a) particles which have never crossed a radius corresponding to twice the initial cut-off radius $R_{\rm cut}$ at any given time (Fig. 7: red line), and (b) all particles that reside within $2 \times R_{\rm cut}$ at any give time (Fig. 7: green line). The oscillations found in the latter case have approximately the same period as that derived from the Lagrange radius L_{98}. A similar behaviour is also found (not shown here) in the previously described runs B1 and C1. We note that the mass loss $f_{\rm ml}(t)$ in all our simulations consists of two main contributions, i.e., an initial exponential decay $f_1(t)$ continuing with a secular linear decay $f_2(t)$:

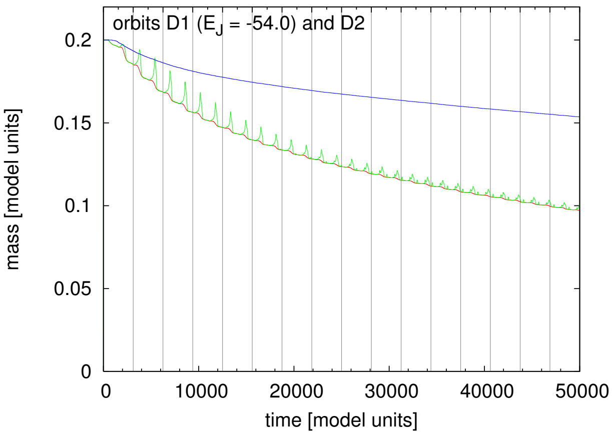

Figure 7. Mass loss from clusters in simulations D1 and D2. Red and blue line: Remaining cluster mass in D1 and D2, respectively, after removing all particles which have ever crossed the sphere around the cluster density centre with radius $2 \times R_{\rm cut}$. Green line: Mass of all particles in D1 that reside within this sphere at the current time.

$$f_{\rm ml}(t) = f_1(t) + f_2(t) = (m_0\, e^{-m_1\, t}) + (m_2 - m_3\, t)\,. \quad (6)$$

We discuss this dependency in more detail in Sec. 3.4. At the end of simulation D1 about 52 percent of the initial cluster mass is gravitational unbound (see Fig. 7), while for the corresponding circular orbit in simulation D2 about 23 per cent of the original cluster mass is unbound.

3.2.4 Simulations E1 and E2

To test our hypothesis of the influence of the stability of the periodic orbits on washing out the tidal tails we chose now an unstable x_1 orbit roughly centred on the instability

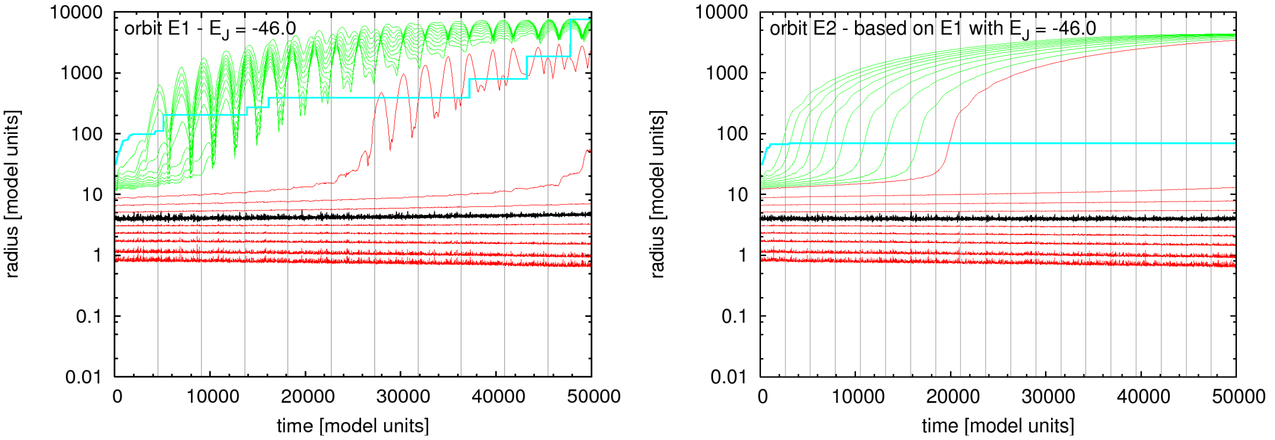

Figure 8. Lagrange radii for the simulation E1 (left panel; cluster on an x_1 orbit with $E_J = -46.0$) and simulation E2 (right panel, cluster on the corresponding circular orbit). The layout of both panels is the same as in Fig. 3.

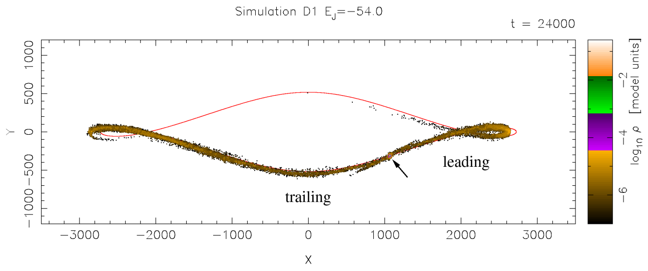

Figure 9. Star cluster in simulation D1 at time $t = 24000$. The particles are coloured according to the local mass density of the cluster. The underlying periodic is shown with a red line. The arrow points to the cluster position. Leading and trailing arms are labelled accordingly.

strip in the characteristic curve between $E_J \approx -48.4$ and -43.6. As in the previous case, this x_1 orbit shows loops close to its apocentres (see Fig. 2). In Fig. 8 we show the evolution of the Lagrange radii for simulations E1 and E2. The initial evolution of the cluster and its tidal tails follow the underlying parent orbit. After a few apocentre passages, however, the structure of the trailing tidal tail becomes more diffusive and even shows multiple tail-like structures (e.g., compare Figs. 9 and 10). Both the leading and the trailing tidal tails wash out after a few apocentre passages, while the cluster on the corresponding run E2 (circular orbit) shows nicely separated tidal tails.

The clusters in E1 and E2 have lost by the end of the simulation about 30 and 17 per cent of the initial cluster mass, respectively. This supports the trend that a star cluster in barred potential loses more mass than the same cluster on the corresponding circular orbit in the axisymmetric case, when being evolved for the same time period.

3.2.5 Simulations F1 and F2

The x_1 orbit in our simulation F1 has peak-like edges at apocentre. The orbit lies right at the knee (kink) of the x_1 characteristic curve in a stable region, but just next to an unstable region (towards larger pericentres).

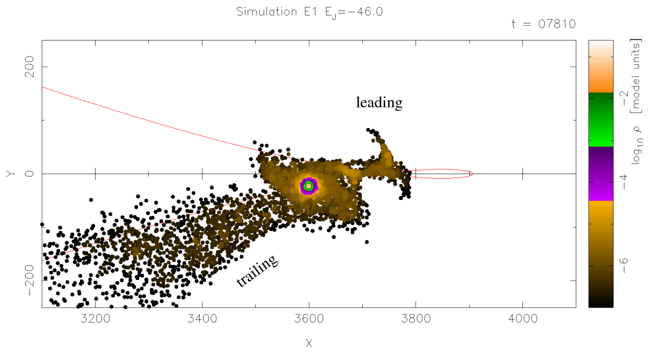

Figure 10. Star cluster in simulation E1 at time $t = 7810$. The particles are coloured according to the local mass density of the cluster. The underlying periodic orbit is shown with a red line.

The formation of the tidal tails and their evolution is similar to that of the previous models. At $t \approx 7300$ the leading tidal tail is highly compressed into one leading clump with distance of $\Delta R \approx 150$. The star cluster in run F1 loses about 11 per cent and in run F2 about 14 per cent of its initial mass.

3.2.6 Simulations G1 and G2

This orbit is a stable x_1 orbit. The formation of the tidal tails is similar to the case of circular orbits. The leading tail slows down when approaching apocentre and the clumpy sub-structure is stronger in this phase. The location of the clumps within the tails changes with time. Indeed, as the clumps in the leading tail slow down when approaching apocentre their relative distance with respect to the cluster centre becomes shorter. At the end of the simulation the tidal tails extend roughly over the underlying periodic orbit. As in the previous runs the centre of mass of the cluster does not stay on the underlying orbit. The star cluster in simulations G1 and G2 loses about 19 and 9 per cent, respectively, of the initial cluster mass.

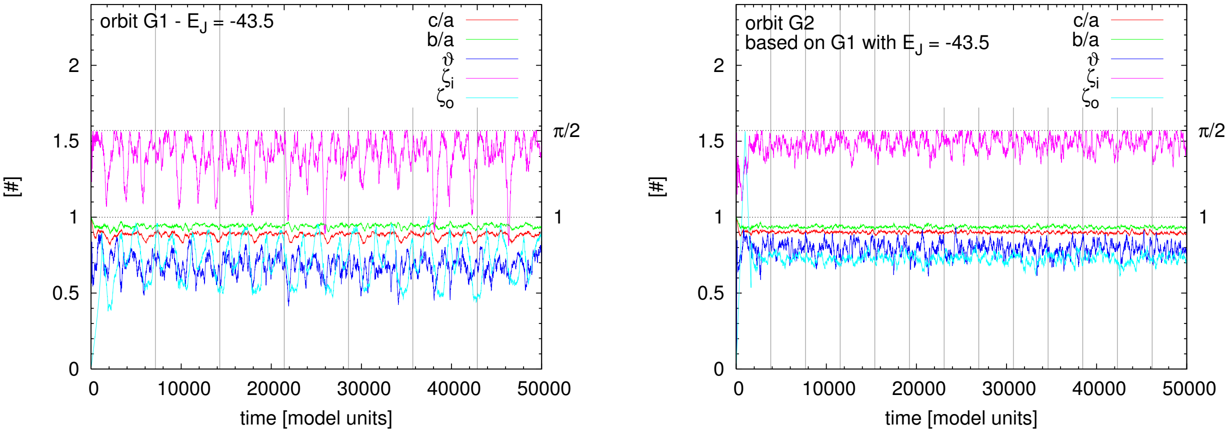

Figure 11. Axial ratios c/a (red line) and b/a (green line) derived from moments of inertia within a spherical shell with $r = 5 \ldots 25$, as well as the corresponding triaxiality parameter ϑ (blue line) as given in Eq. 7. We also show the angle between the clusters centre of mass velocity vector and the major axis unit vector based on the moments of inertia measured (a) in shells with $r = 5 \ldots 25$ (ζ_i; magenta line) and (b) with $r = 100 - 150$ (ζ_o; cyan line). Left panel: results from run G1. Right panel: results from run G2.

3.2.7 Simulations H1 and H2

The orbit in simulation H1 is a 4/1 orbit, i.e., a four-periodic orbit closing after one rotation and four radial oscillations. It is an unstable orbit and has sharp pointy edges at its apocentres. As before, we witness the formation of tidal tails, which after apocentre passages do not follow the underlying orbit anymore. The evolution of the star cluster in this run further supports our hypothesis that the orbit stability in the global galactic potential determines the orientation and shape of the tidal tails and also how diffusive they are. The cluster in run H2, i.e., on the corresponding circular orbit, does not show any peculiarities as compared to the earlier simulations using circular orbits. The mass loss at the end of the simulation is about 8 per cent in run H1 and about 4 per cent in run H2.

3.2.8 Simulations J1 and J2

This orbit in simulation J1 is again an unstable 4/1 orbit. In contrast to the previous orbit H1, however, it has loops at its apocentres. The tidal tails which form in this model are initially aligned with the underlying periodic orbit. This changes after the first apocentre passage, when reaching the outer edge of the loop there. The tail rapidly swings around when the cluster runs through the loop and aligns again with the orbit after the cluster leaves the loop. After the third apocentre passage the tidal tails are less sharply defined and less aligned with the periodic orbit. As in the other cases with unstable orbits, the tidal tails slowly dissolve into a very diffusive morphology. We furthermore note that the cluster itself does not remain centred on the initial periodic orbit, but its density centre reaches separations up to $\Delta R \approx 100$ from the initial underlying periodic orbit.

Both the mass loss rate of the cluster and the density in the tidal tails is relatively low. At the end of the run the tidal tails have filled about half the underlying orbit. In simulation J1 the star cluster loses about 11 per cent of its initial mass and about 5 per cent in run J2.

3.3 Shape and orientation of the cluster

In order to quantify the shape and orientation of both the cluster and the tidal tails formed in the simulations, we calculate the moments of inertia tensor of the cluster inside a spherical shell within $5 \geqslant r \geqslant 25$ and determine the corresponding set of eigenvalues I_a, I_b, I_c, with $I_a \leqslant I_b \leqslant I_c$. For the analysis we use the EISPACK software package (Smith et al. 1976). From the eigenvalues we then determine the axial ratios as $b/a = \sqrt{(I_c + I_a - I_b)/(I_c + I_b - I_a)}$ and $c/a = \sqrt{(I_b + I_a - I_c)/(I_c + I_b - I_a)}$ as well as the triaxiality parameter as defined, e.g., in Franx et al. (1991), as

$$\vartheta = (1 - b^2/a^2)/(1 - c^2/a^2) , \tag{7}$$

with $a > b > c$. In terms of the eigenvalues, Eq. 7 can also be rewritten as $\vartheta = (I_b - I_a)/(I_c - I_a)$. This definition gives $\vartheta = 1$ for a prolate object ($a > b = c$; cigar-like shape) and $\vartheta = 0$ for an oblate object ($a = b > c$; disc-like shape). An example of the time evolution of ϑ is shown in Fig. 11 (left panel; blue line). We find that star clusters on orbits in barred potentials and high energies $E_{\rm J}$ typically have smaller triaxiality parameter ϑ, while clusters on orbits with smaller energy $E_{\rm J}$ have values of $\vartheta \approx 1$.

Furthermore, we determine the angles ζ_i between the current centre of mass velocity vector of the cluster and the major axis inertia eigenvector determined from the mass distribution of the cluster within a spherical shell between $r = 5$ and 25. Similarly we define ζ_o using the corresponding eigenvector for the tidal tails (measured between $r = 100$ and 150). Fig. 11 (right panel) shows the results for the circular orbit G2. Once the tidal tails have formed, the axial ratios of the cluster remain roughly constant. From the moments of inertia we find that the cluster is elongated perpendicular (i.e., $\zeta_i \approx 0.5\pi$) to its trajectory (due to the radial tidal force). The tidal tails follow the underlying orbit. Within the region r=100 and 150 (which is relatively close to the cluster compared to the total length of the tails) we get $\zeta_o \approx 0.25\pi$ for our run G2.

For orbits in barred potential (see Fig. 11, left panel)

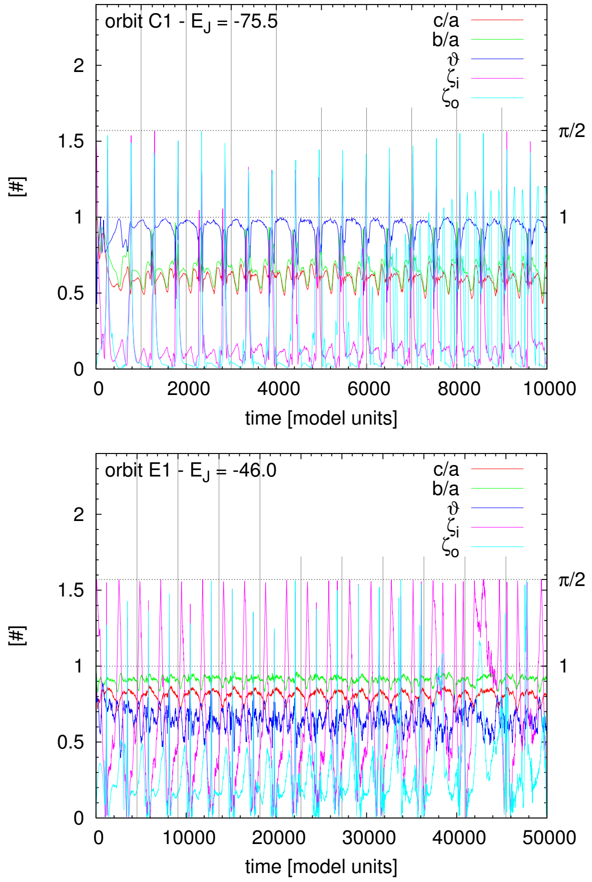

Figure 12. Results from our simulations C1 (top panel) and E1 (bottom panel). The layout is the same as in Fig. 11.

the semi-major axis of the cluster lies in the orbital plane but periodically changes its orientation within the orbital plane with respect to the cluster trajectory. The same is true for the tidal tails. The oscillations of ζ_o have a larger amplitude than those of ζ_i. The evolution of the orientation of both the cluster and tidal tails is more regular as compared to orbits in the barred potential. We note that the amplitude of the oscillations in ζ_o are higher for orbits which have large variations in their radius of curvature (compare Fig. 12).

In Fig. 13 we plot the time-averaged values of the axial ratios $< c/a >$ and $< b/a >$, as well as of the triaxiality parameter $< \vartheta >$, all as a function of the Jacobi integral $E_{\rm J}$ of the underlying periodic orbit. We find that star clusters at larger $E_{\rm J}$ roughly maintain their spherical symmetry, much more so than clusters on orbits with small $E_{\rm J}$ (i.e. clusters near the centre), which become considerably triaxial. Clusters nearer to the centre also have larger dispersions of their axial ratios. The *flattening* ¡c/a¿ of the cluster follows the same trend for simulations in barred and in axisymmetric potentials. This is not true for the *elongation* ¡b/a¿ in the orbital plane, which has a stronger dependence on $E_{\rm J}$ in barred than in non-barred cases. These effects are presumably the reflections of the variation of the tidal force along the corresponding periodic orbit.

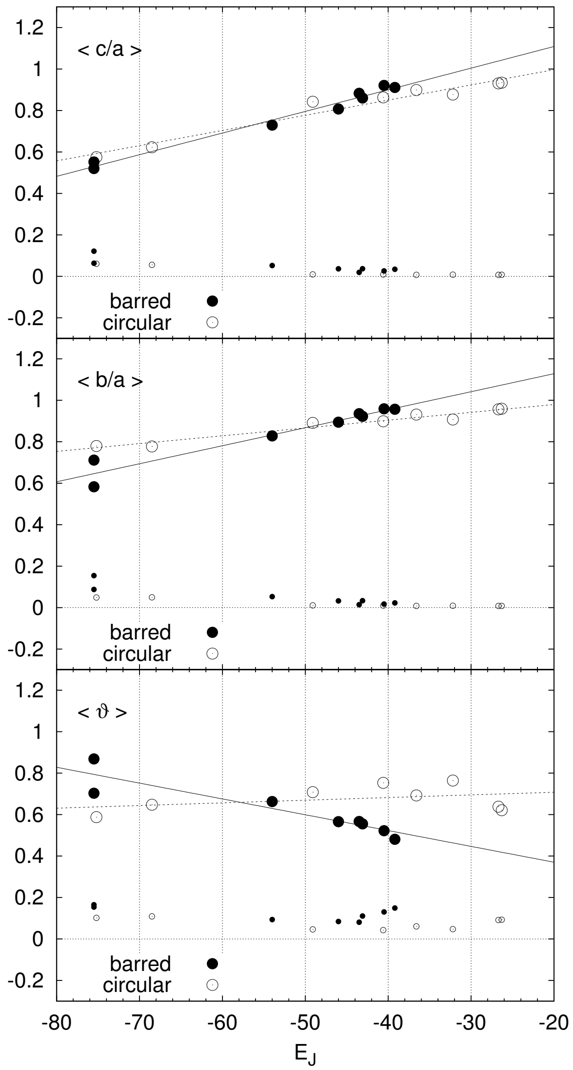

Figure 13. Time-averaged axial ratios $< c/a >$ (top panel), $< b/a >$ (middle panel) and triaxiality parameter $< \vartheta >$. The filled and open symbols represent simulations with barred orbits and circular orbits, respectively. The corresponding small symbols show the standard deviation, of these quantities.

3.4 Tidal forces

To quantify the strength of the tidal forcing along the periodic orbits we calculate the eigenvalues (q_1, q_2, q_3) and the corresponding eigenvectors of the force tensor[3], as given by

$$Q_{ij} = \frac{\partial^2 \Phi_{\rm gal}}{\partial x^i \partial x^j} \, . \qquad (8)$$

We find that one of the eigenvectors is always parallel to the z-axis, i.e., oriented perpendicular to the orbital plane. In the following we call the corresponding eigenvalue q_z and the two remaining eigenvalues q_a and q_b. The eigenvectors

---

[3] This definition is similar to that of the tidal tensor used in, e.g., Renaud et al. (2008) and Pasetto & Chiosi (2009).

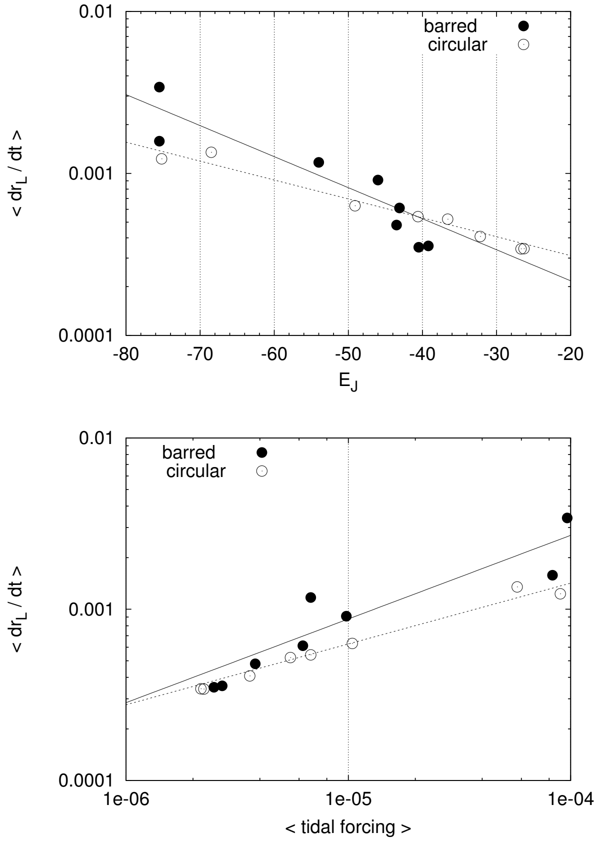

Figure 14. Cluster expansion rate based on a linear fit to the (logarithmic) Lagrange radii of the outer mass shells. Filled and open symbols indicate simulations in barred and unbarred potentials, respectively.

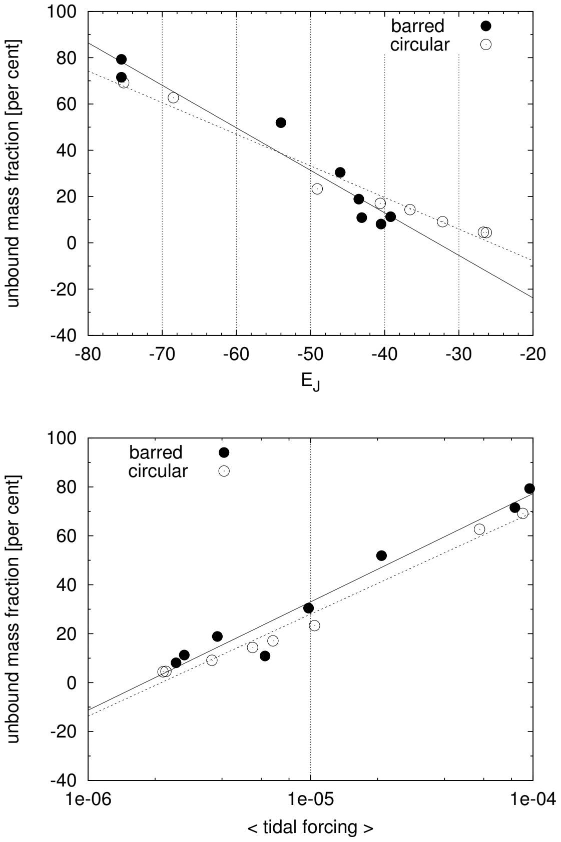

Figure 16. Final mass loss (in per cent) in unbound material. Filled and open symbols indicate simulations in barred and unbarred potentials, respectively.

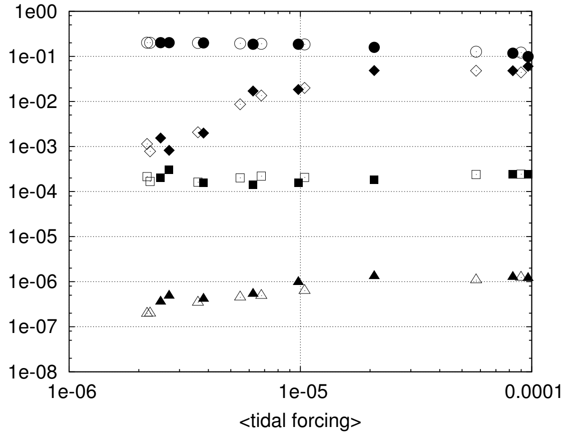

Figure 15. Mass loss parameters as a function of the average tidal forcing. Filled and open symbols represent simulations in barred and axisymmetric potentials, respectively. The parameter of the linear fit $f_2(t) = m_2 - m_3\, t$ are plotted with circles (m_2) and triangles (m_3). The parameter of the exponential fit $f_1(t) = m_0 e^{-m_1\, t}$ are plotted with diamonds (m_0) and squares (m_1).

of q_a and q_b lie within the orbital plane. Positive eigenvalues are found for expansive flows, while negative ones represent for compressive flows. We measure the *tidal forcing* on the cluster by the quantity $\sqrt{q_a^2 + q_b^2}$. In Fig.2 we use this quantity for the colour coding of the orbits. Note that the tidal forcing in barred potentials is strongest along the bars intermediate axis $b_{\rm bar}$ for our simulations with $E_{\rm J} \leqslant -43.1$ and along the bars major axis $a_{\rm bar}$ otherwise.

As can be seen in the figures showing Lagrange radii, the expansion rate of the different mass shells typically seems to be higher for orbits in the barred potential as compared to the circular ones. In Fig. 14 we show the rate at which the cluster is expanding/dissolving. We determine this rate by using a linear fit to the steeply rising part of the Lagrange radii of the outer mass shells. We then calculate the average expansion rate $< dr_{\rm L}/dt >$ for each run from about 5 determined slopes. The top panel in Fig. 14 shows the expansion rate as a function of the Jacobi integral $E_{\rm J}$. We find a strong correlation between the expansion rate and the Jacobi integral. Equivalently, we also plot the expansion rate as a function of the orbit-averaged[4] *tidal forcing* (see bottom panel in Fig. 14). Generally, the expansion rate is found to be higher for clusters in barred potentials (at least for small $E_{\rm J}$).

---

[4] See Sec. 3.1 for details.

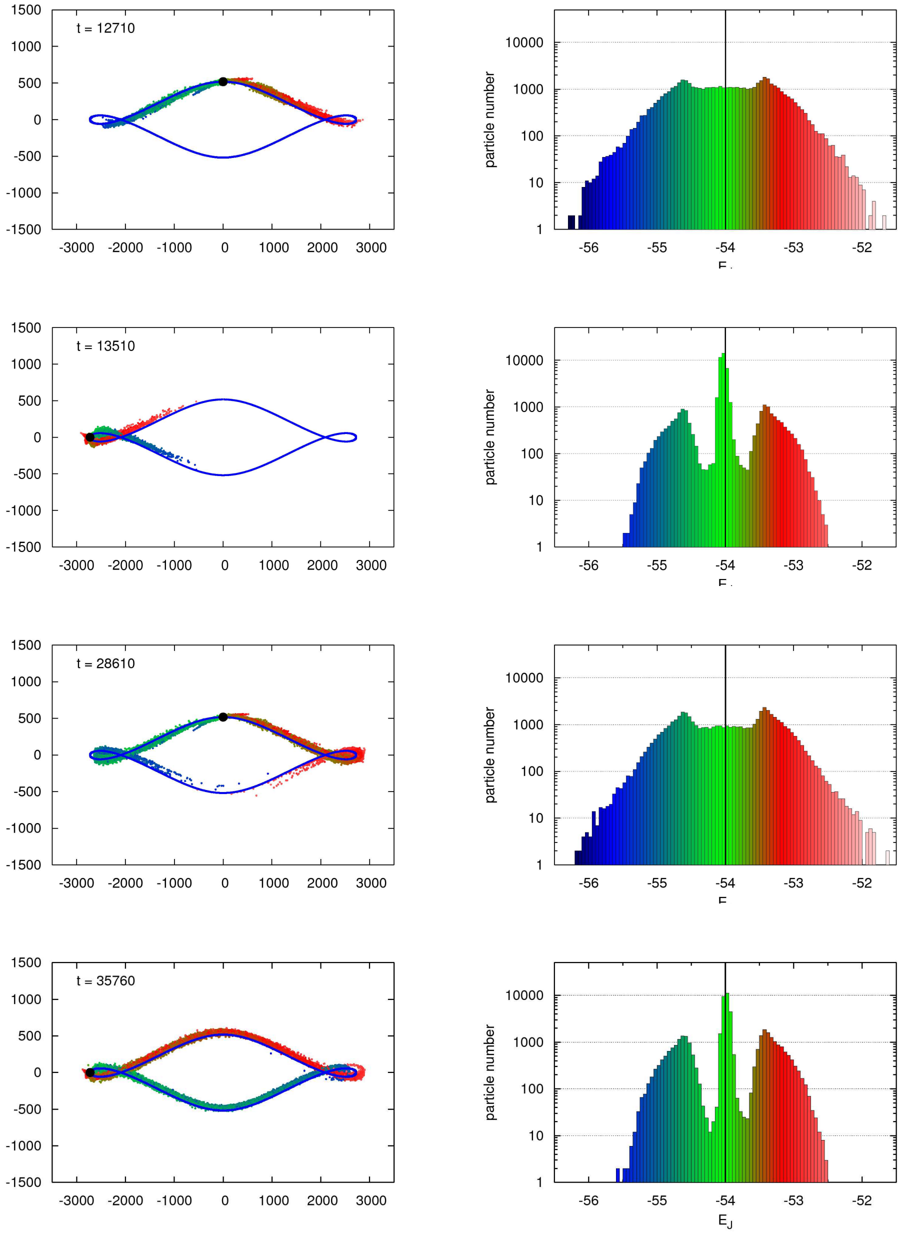

Figure 17. Distribution of Jacobi energy $E_{\rm J}$ for simulation D1. The times from top to bottom correspond to 16, $16\,{}^1\!/_4$, 36, and $44\,{}^1\!/_4$ orbital periods, respectively. The left panels show the projected particle distribution colour coded by $E_{\rm J}$. The underlying periodic orbit is shown by the blue line and the position of the cluster is marked with a black dot. The right panels show the binned $E_{\rm J}$ distribution using the same colour coding as before. The Jacobi integral of the underlying periodic orbit is indicated by the vertical thick line.

In all our simulations the clusters lose their mass (i.e., stars become gravitationally unbound) roughly linearly. For clusters starting close to the centre of the galaxy, we observe an additional, exponentially decaying mass loss, as a consequence of the non-equilibrium initial conditions of the cluster in the strong tidal field of the galaxy. To quantify the mass loss of the clusters in our simulations, we fit $f_{\rm ml}$ from our Eq. 6 to the mass as a function of time curves, such as shown in Fig. 7. The results of these fits is shown in Fig. 15. For simulations with a weak tidal forcing we get a y-intercept of the linear contribution of $m_2 = 0.2$, which corresponds to the initial cluster mass. This shows that, in this case, there is no significant contribution from the exponential mass loss. For higher values of the tidal forcing (and the initial tidal perturbation), the exponential part $f_1(t)$ becomes more and more important. At the same time, the value of m_2 drops to roughly 0.1. The linear mass loss rate (m_3), shown as triangles in Fig. 15, increases with increasing tidal forces. The solid triangles (barred models) lie slightly higher than the open ones (axisymmetric potential).

The exponential mass loss rate m_1 (squares) is roughly independent of the tidal forcing, but the amplitude m_0 (diamonds) increases considerably with increasing tidal forcing. To summarise, it seems that if we compare clusters in barred and axisymmetric potentials that there is on average very little difference in the overall mass loss rate, if the average tidal forcing along the orbits is the same.

In Fig. 16 we show the total mass loss of the cluster determined at the end of the simulations. We again find strong correlations between this mass loss and the Jacobi integrals of the orbits or the average tidal forcing.

3.5 Energy considerations

In Figures 17 we show the evolution of the energy distribution within the cluster for simulations D1 (barred potential). This is of particular interest concerning the interpretation of observational data on the virial state of a star cluster (Küpper et al. 2011), e.g., such as Palomar 13.

Fig. 17 shows the particle distribution in simulation D1 (left panels) and the corresponding energy distribution (right panels), both with a colour scheme based on their Jacobi integral. The snapshots are chosen at times when the cluster is at apo- (second and fourth rows) and peri-centre (first and third rows). With the formation of the tidal tails and the accompanied dissolution of the main cluster body the energy distribution slowly forms a double peak structure roughly symmetric with respect to the Jacobi integral of the periodic orbit. Thus the whole distribution has a three peak structure: the two peaks corresponding to the tidal tails, plus the central peak of the initial cluster distribution. The latter can at times be relatively low, so that the central structure may look like a plateau, particularly with the logarithmic scale we are using. At pericentres the double peaks reach higher values than at apocentres. However, the relative contrast between the peaks becomes much strongest at apocentres, so that they stand out clearest. This is due to the compression effect described in Sect. 3.2.1. Note that the central peak is not pronounced at pericentres, but stands out clearly at apocentres, where it is an order of magnitude higher than at pericentre. Comparing these structures always at the same phase of the orbit (i.e. always at apocentre, or always at pericentre) we find that, as time increases, the height of the two side peaks increases, that of the central peak decreases and the contrast between the peaks becomes much sharper. This is due to the fact that more and more material leaves the cluster and moves to the tails, as seen in Sect. 3.

Note that the double peak structure mentioned above is also visible in simulations with circular orbits, but is nevertheless much less pronounced - due to the absence of the compression/expansion along the circular orbit. Further discussion of the tails and of the corresponding $E_{\rm J}$ distributions will be given elsewhere (Athanassoula, Rómero-Gomez and Berentzen, in prep.).

4 SUMMARY AND CONCLUSIONS

Stellar streams are fossils of the formation history of galaxies and can be used to reconstruct, e.g., the shape of the gravitational potential of dark matter halos. Several issues such as the life-time of the clusters and their tidal streams however are not yet fully understood. The understanding of the morphology and the dynamics of the tails and their sub-structures is still in its infancy. Numerical N-body simulations are a main key to address these questions. Many simulations in the literature focus on the evolution of dense stellar systems in an external axisymmetric potential on both circular and eccentric orbits, respectively. For orbits close to the galactic plane, however, non-axisymmetric perturbations in the disk, such as stellar bars and/or spiral arms, are expected to significantly influence the dynamical evolution of star clusters.

In this work we have presented a set of direct N-body simulations of star clusters orbiting in the plane of a barred galaxy potential. The clusters are placed in the mid-plane of the galactic disc and launched on periodic orbits which have been selected from the main planar 2-d families. The results are then compared to the evolution of star clusters on circular orbits in an axisymmetric potential.

We find that the star clusters dissolve due to the tidal force field of the galaxy – in both the axisymmetric as well as in the barred potential. While the tidal tails in the axisymmetric potential continuously grow in length, we find a periodic compression and expansion of the tails for star clusters in the barred potential. Both the length and the density of the tidal tails vary with time and are directly correlated to orbital period of the underlying parental orbit. We find sub-structures within the tidal tails in form of clumps (or epicyclic over-densities). The qualitative evolution of these structures is in agreement with the results of Küpper et al. (2010), who studied the evolution of star clusters on eccentric orbits in a static axisymmetric potential.

We also studied the distribution of the Jacobi energy $E_{\rm J}$ of the cluster stars and found that it depends strongly on the location of the cluster along the orbit. It remains, nevertheless, roughly symmetrical with respect to the Jacobi energy of the cluster orbit. Two peaks develop, one on each side of this energy, and their relative amplitude depends on the location of the cluster along the orbit. At apocentres the distribution is tri-modal and the three peaks are very clearly separated. At pericentres, the distribution is much more extended and the central peak is not clearly delineated.

We find that the mass loss of the cluster is mainly determined by the orbit-averaged tidal forcing. In other words, the shape of the gravitational potential – at least in the case studied here – affects the dissolution time-scale only very little. On the other hand, the stellar bar has a strong effect on the shape and morphological evolution of the tidal tails: the stability of the orbit has a strong impact on how long the tidal tails and their sub-structures actually survive. This makes it more subtle to reconstruct the cluster orbits in observations and thus to probe that galactic potential in the disc plane. This could also be the case small galactic altitudes in which the 3-d shape of orbits is strongly affected by the stellar bar (e.g., Pfenniger 1984; Berentzen et al. 1998; Skokos et al. 2002a, b; Patsis et al. 2002).

ACKNOWLEDGMENTS

We would like to thank the anonymous referee for her/his comments and suggestions which helped to improve the manuscript. We also would like to thank Rainer Spurzem, Andreas Just, Peter Berczik, Andreas Ernst and Albert Bosma for many fruitful discussions. We are grateful to Jean-Charles Lambert for his most valuable help and assistance. IB acknowledges the kind hospitality and the support from the Observatory Astronomique de Marseille-Provence during his visit in which this work has been initiated. He also acknowledges funding through the University of Marseille for his visit. Furthermore, IB acknowledges funding through a Frontier Innovation grant of the University of Heidelberg sponsored by the German Excellence Initiative, as well as funding by the Sonderforschungsbereich SFB 881 "The Milky Way System" (subproject A1) of the German Research Foundation (DFG). The Kolob GPU Cluster used for most simulations in this work is funded in part by the DFG via Emmy-Noether grant BA 3706.

REFERENCES

Athanassoula, E., 1992, MNRAS, 259, 328
Belokurov, V., Evans, N.W., Irwin, M.J., Hewett, P.C., Wilkinson, M.I., 2006, ApJ, 637, L29
Berczik, P., Merritt, D., Spurzem, R., 2005, ApJ, 633, 680
Berczik, P., Merritt, D., Spurzem, R., Bischof, H.-P., 2006, ApJ, 642, L21
Berentzen, I., Heller, C.H., Shlosman, I., Fricke, K.J., 1998, MNRAS, 300, 49
Berentzen, I., Preto, M., Berczik, P., Merritt, D., Spurzem, R., 2009, ApJ, 695, 455
Binney, J., Tremaine, S., 1984, Galactic Dynmics, Princeton Univ. Press, NJ
Contopoulos, G., Papayannopoulos, Th., 1980, A&A, 92, 33
Dehnen, W., 2000, ApJ, 536, L39
Dehnen, W., 2002, JCP, 179, 27
Ernst, A., Just, A., Spurzem, R., 2009, MNRAS, 399, 141
Ferrers, N. M., 1877, in: "An elementary treatise on spherical harmonics and subjects connected with them". Macmillan and co. (London)
Franx, M., Illingworth, G., de Zeeuw, T., 1991, ApJ, 383, 112
Fukushige T., Makino J., Kawai A., 2005, PASJ, 57, 1009
Gaburov E., Harfst S., Portegies Zwart S.F., 2009, New Astronomy, 14, 630
Gieles M., Portegies Zwart S.F., Baumgardt H., Athanassoula E., Lamers H.J.G.L.M., Sipior M., Leenaarts J., 2006, MNRAS, 371, 793
Gieles M., Athanassoula E., Portegies-Zwart S., 2007, MNRAS, 376, 809
Grillmair, C.J., 2009, ApJ, 693, 1118
Harfst S., Gualandris A., Merritt D., Spurzem R., Portegies Zwart S., Berczik P., 2007, New Astronomy, 12, 357
Heller, C.H., Shlosman, I., 1996, ApJ, 471, 143
Just, A., Khan, F.M., Berczik, P., Ernst, A., Spurzem, R., 2011, MNRAS, 411, 653
Khalisi, E., Amaro-Seoane, P., Spurzem, R., 2007, MNRAS, 374, 703
Kharchenko, N.V., Berczik, P., Petrov, M.I., Piskunov, A.E., Röser, S., Schilbach, E., Scholz, R.-D., 2009, A&A, 495, 807
King, I. R., 1966, AJ, 71, 64
Küpper, A.H., Macleod, A., Heggie, D.C., 2008, MNRAS, 387, 1248
Küpper, A.H., Mieske, S., Kroupa, P., 2011, MNRAS, 413, 863
Küpper, A.H., Kroupa, P., Baumgardt, H., Heggie, D.C., 2010, MNRAS, 401, 105
Makino, J., Aarseth, S.J., 1992, PASJ 44, 141
Makino, J., Fukushige T., Koga, M., Namura, K., 2003, PASJ, 55, 1163
Martínez-Delgado, D., Pohlen, M., Gabany, R.J., Majewski, S.R., Peñarrubia, J., Palma. C, 2009, ApJ, 692, 955
Martínez-Delgado, D., Gabany, R.J. Crawford, K., and 12 co-authros, 2010, AJ, 140, 942
Miyamoto, M., Nagai, R., 1975, PASJ, 27, 533
Odenkirchen, M., Grebel, E.K., Rockosi, C.M., Dehnen, W., and 16 coauthors, 2001, ApJ, 548, L165
Pasetto, S., Chiosi, C., 2009, A&A, 499, 385
Pfenniger D., A&A, 1984, 134, 373
Patsis, P., Skokos, Ch., Athanassoula, E., 2002, MNRAS, 342, 69
Peng, E.W., Ford, H.C., Freeman, K.C., White, R., 2002, AJ, 124, 3144
Plummer, H.C., MNRAS, 71, 460
Renaud, F., Boily, C.M., Fleck, J.-J., Naab, T., Theis, Ch., 2008, MNRAS, 391, L98
Sellwood, J.A., Wilkinson, A., 1993, Reports on Progress in Physics, 56, 173
Skokos, Ch., Patsis, P.A., Athanassoula, E., 2002a, MNRAS, 333, 847
Skokos, Ch., Patsis, P.A., Athanassoula, E., 2002b, MNRAS, 333, 861
Smith, B.T., Boyle, J.M., Dongarra, J. J., 1976, Matrix Eigensystem routines - Eispack guide, in: Lecture Notes in Computer Science, Berlin:Springer, 2nd ed.
Teuben, P.J., 1995, The Stellar Dynamics Toolbox NEMO, in: Astronomical Data Analysis Software and Systems IV, ed., R. Shaw, H.E. Payne and J.J.E. Hayes (1995), PASP Conf. Series 77, p. 398
Varghese, A., Ibata, R., Lewis, G.F., 2011, MNRAS, in press (arXiv:1106.1765)

This paper has been typeset from a TEX/ LATEX file prepared by the author.